

# The symbiotic binary St 2-22: Orbital and stellar parameters and jet evolution following its 2019 outburst

Gałań C.<sup>1</sup>, Mikołajewska J.<sup>1</sup>, Ilkiewicz K.<sup>2</sup>, Monard B.<sup>3</sup>, Żywica S. T.<sup>4</sup>, and Zamanov R. K.<sup>5</sup>

<sup>1</sup> Nicolaus Copernicus Astronomical Center, Polish Academy of Sciences, Bartycka 18, 00-716 Warsaw, Poland  
e-mail: cgaalan@camk.edu.pl

<sup>2</sup> Centre for Extragalactic Astronomy, Department of Physics, University of Durham, South Road, Durham DH1 3LE, UK

<sup>3</sup> Kleinkaroo Observatory, Calitzdorp, Western Cape, South Africa

<sup>4</sup> Institute of Astronomy, Faculty of Physics, Astronomy and Informatics, Nicolaus Copernicus University in Toruń, Grudziądzka 5, Toruń 87-100, Poland

<sup>5</sup> Institute of Astronomy and National Astronomical Observatory, Bulgarian Academy of Sciences, Tsarigradsko Shose 72, 1784 Sofia, Bulgaria

Received 3 September 2021 / Accepted 22 October 2021

## ABSTRACT

**Context.** St 2-22 is a relatively poorly studied S-type symbiotic system that belongs to a small group of jet-producing systems as a result of disc accretion onto a white dwarf fed by its red giant companion.

**Aims.** The goal of this paper is to analyse the nature and derive the basic parameters of St 2-22, and to follow the jet evolution.

**Methods.** Photometric monitoring for over 16 yrs and high-quality spectroscopic data enabled us to shed new light on its nature. The high-resolution SALT spectra and  $V I_C$  photometry obtained during and between the last two outbursts have been used to search for periodic changes, to derive spectroscopic orbits of both system components, and to study the outburst and jet evolution.

**Results.** We present the orbital and stellar parameters of the system components. The orbital period is  $P_{\text{orb}} = 918 \pm 6^{\text{d}}$ . The double-line spectroscopic orbits indicate the mass ratio  $q = M_g M_h^{-1} = 3.50 \pm 0.53$ , and the components masses  $M_g \sin^3 i \sim 2.35 M_\odot$  and  $M_h \sin^3 i \sim 0.67 M_\odot$ . The orbit shows significant eccentricity,  $e = 0.16 \pm 0.07$ . The orbital inclination is close to  $70^\circ$ . During outbursts, accelerating and decelerating jets are observed with changes in their radial velocity component in a range from  $\sim 1500$  up to nearly  $1800 \text{ km s}^{-1}$ . St 2-22 turned out to be a classical symbiotic system very similar to the precursor of the group – Z And.

**Key words.** binaries: symbiotic – stars: jets – novae, cataclysmic variables – stars: – individual: St 2-22 (PN Sa 3-22)

## 1. Introduction

St 2-22 = PN Sa 3-22 ( $\alpha_{2000}$ :  $13^{\text{h}} 14^{\text{m}} 30.3^{\text{s}}$ ,  $\delta_{2000}$ :  $-58^\circ 51' 49.6''$ ) is a poorly studied classical symbiotic binary, composed of an  $\sim M4$ -type red giant (RG) and a hot accreting white dwarf (WD). It is one of a handful of symbiotic systems (SySt) known to produce high-velocity ( $\sim \text{a few } \times 10^3 \text{ km s}^{-1}$ ) collimated jets during their outbursts (Tomov et al. 2017). However, so far only one outburst has been recorded with only two spectra taken during it, and many issues have yet to be addressed.

Initially, the object was classified as a planetary nebula (Sanduleak 1976), but the object was reclassified as SySt by Allen (1984) who identified the Raman scattered  $\text{O VI } 6825 \text{ \AA}$  line in its spectrum. Van Winckel et al. (1993) reported brightness variations at the end of the 1980s and the beginning of the 1990s, however without details about their nature. A search for linear polarisation by García et al. (2003) gave a negative result. Zamanov et al. (2008) included St 2-22 in their studies of rotational velocities of the RGs in SySt. Mürset & Schmid (1999) estimated an M4.5 spectral type for the RG. Mikołajewska et al. (1997) estimated the distance  $\sim 5 \text{ kpc}$  as well as the temperature  $T_h \sim 54\text{--}100 \times 10^3 \text{ K}$  and luminosity  $L_h \sim 600 L_\odot$  of the WD. Collimated, bipolar jets with an average velocity of  $\sim 1700 \text{ km s}^{-1}$  were discovered in spectra collected during an unnoticed outburst in 2005 (Tomov et al. 2017). The nature of the outburst

was similar to those observed in classical SySt. The chemical composition and physical parameters of the RG,  $[\text{O III}]$  emission line ratios, and infrared colours of St 2-22 are consistent with an S-type SySt (Tomov et al. 2017).

At the beginning of 2019, another eruption began that is still ongoing. Here we discuss the characteristics of the last outburst phenomenon and evolution of jets. We also provide the orbital and physical parameters of St 2-22 based on spectra collected around the last two outbursts.

## 2. Observations

### 2.1. Spectra

High-resolution ( $R \sim 40000$ ; range:  $3920\text{--}8780 \text{ \AA}$ ) spectra were collected with the Southern African Large Telescope (SALT) High Resolution Spectrograph (HRS) in medium-resolution mode under programmes 2018-2-SCI-021 and 2019-1-MLT-008 (PI: C. Gałań). These data are complemented with publicly available, HRS spectra acquired in low-resolution mode ( $R \sim 14000$ ; useful range:  $4000\text{--}8790 \text{ \AA}$ ) under programmes 2017-1-SCI-046 and 2017-2-SCI-044 (PI: T. Tomov). In this case, three exposures were collected for each night which have been finally summed into single spectra. The HRS observations were reduced using the MIDAS-based pipeline<sup>1</sup> (Kniazev

<sup>1</sup> [http://www.sao.ac.za/~akniazev/pub/HRS\\_MIDAS/HRS\\_pipeline.pdf](http://www.sao.ac.za/~akniazev/pub/HRS_MIDAS/HRS_pipeline.pdf)

**Table 1.** Heliocentric radial velocities of the red giant and the cF-absorption lines with their  $1\sigma$  errors, and the maximum  $IP$  observed.

Date [UT] yyyy-mm-dd	HJD -2450000	Phase*	$IP_{\max}$ [eV]	$RV_{\text{cool}}$ [km s <sup>-1</sup> ]	$RV_{\text{cF}}$ [km s <sup>-1</sup> ]
2005-02-01	3402.8	0.272	55	$37.98 \pm 0.32$	—
2005-05-16	3506.6	0.385	99	$36.46 \pm 0.37$	—
2017-04-17	7861.3	0.129	114	$36.24 \pm 0.69$	—
2017-05-10	7884.5	0.154	114	$39.28 \pm 1.00$	—
2017-06-12	7917.4	0.190	114	$40.01 \pm 0.64$	—
2017-07-06	7941.3	0.216	114	$37.82 \pm 0.67$	—
2017-07-30	7965.3	0.242	114	$39.55 \pm 0.69$	—
2018-02-05	8154.5	0.448	114	$33.32 \pm 0.76$	—
2018-03-04	8182.4	0.479	114	$30.21 \pm 1.25$	—
2019-02-15	8530.5	0.858	55	$25.91 \pm 0.68$	$55.6 \pm 1.3$
2019-03-30	8572.6	0.904	25	$26.75 \pm 0.49$	$56.8 \pm 1.3$
2019-05-01	8605.5	0.940	25	$29.01 \pm 0.33$	$49.4 \pm 1.9$
2019-06-08	8643.4	0.981	25	$31.26 \pm 0.44$	$30.7 \pm 1.5$
2020-01-28	8876.5	0.235	55	$39.44 \pm 0.49$	$11.2 \pm 0.7$
2020-05-10	8980.5	0.348	55	$36.29 \pm 0.50$	$15.2 \pm 1.0$
2020-07-01	9032.3	0.404	55	$35.40 \pm 0.43$	$16.1 \pm 1.1$
2021-02-04	9249.5	0.641	55	$29.54 \pm 0.64$	$47.8 \pm 2.8$
2021-03-26	9300.4	0.697	55	$26.22 \pm 0.43$	$55.5 \pm 2.3$
2021-05-02	9337.3	0.737	55	$24.17 \pm 0.37$	$50.3 \pm 0.8$
2021-07-25	9421.3	0.828	55	$25.02 \pm 0.47$	—

**Notes.** (\*) Phase according to the ephemeris:  $HJD_{T_0} = 2458661 + 918 \times E$  (Table 3).

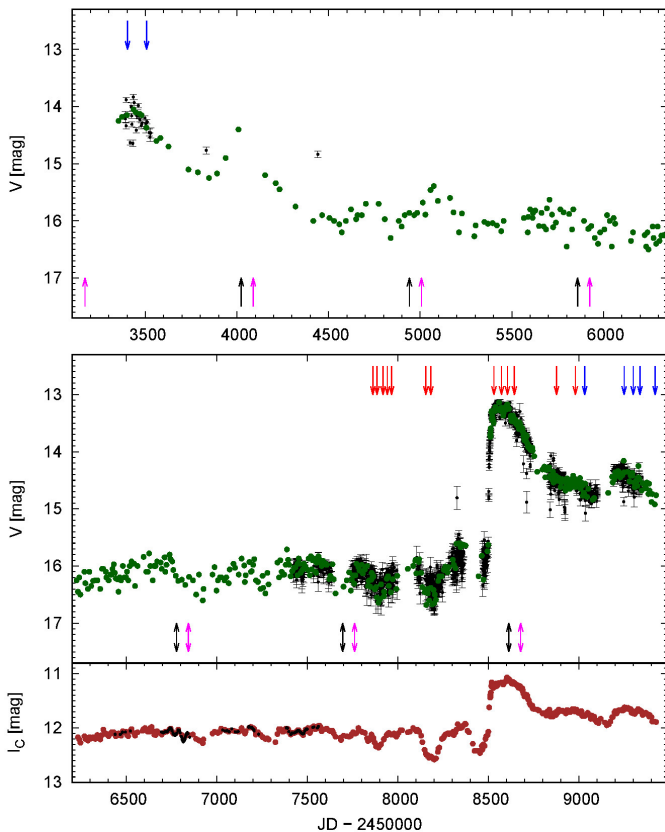


**Fig. 1.** Light curve of St 2-22 with the ongoing outburst. Green and brown dots correspond to the  $V$ - and  $I_C$ -band data, respectively, acquired at the Kleinkaroo Observatory, whereas the ASAS and ASAS-SN  $V$ - and  $g$ -band, as well as *OGLE*  $I$ -band data, are plotted as black points. The zero-point of the *OGLE* photometry is shifted by  $-0.38$  mag. Arrows above the light curves mark the *HRS* and *FEROS* observations with (blue) and without (red) jet detection, while those below mark the times of periastron passage (black) and inferior conjunction (magenta) according to the eccentric orbit solution (Table 3).

2016; Kniazev et al. 2017). We also used four high-resolution (R

$\sim 48000$ ;  $3710\text{--}9215\text{ \AA}$ ) *FEROS* spectra obtained with the 2.2-m MPG/ESO telescope at La Silla Observatory under the programme 074.D-0114. The journal of our spectroscopic observations is presented in Table 1.

## 2.2. Photometry

St 2-22 was monitored for over 16 years starting in December 2004 (JD 2453353) with a 35 cm Meade RCX400 telescope equipped with an SBIG ST8-XME CCD camera and  $V$  and  $I_C$  (beginning in November 2012; JD 2456232) filters at the Kleinkaroo Observatory (South Africa). Each single data point is the result of several individual exposures, which were calibrated (dark subtraction and flat-fielding) and stacked selectively. Magnitudes were derived from differential photometry to nearby reference stars using the single image mode of AIP4 image processing software. Our photometry was supplemented by the data in  $V$  and  $g$  filters from the All Sky Automated Survey for Supernovae (ASAS-SN, Shappee et al. 2014; Kochanek et al. 2017) and by *OGLE*  $I$ -band measurements (see Tomov et al. 2017). Moreover, the  $V$ -band data collected by the ASAS survey (Pojmański 1997) are used for comparison. The light curves are shown in Fig. 1 with arrows marking the times of our spectroscopic observations.

## 3. Results and discussion

### 3.1. Optical light curves

The light curves of St 2-22 show a systematic brightness decline (by  $\Delta V \sim 2$  over  $\sim 2000$  days) followed by about 10 yrs of a stable  $V \sim 16$  with moderate periodic-like fluctuations, and with a major outburst around JD 24558505 (January 21, 2019) that is still ongoing. This outburst began with a steep brightening by  $\Delta V \sim 2^m$  ( $\Delta I \sim 0.7$ ) in  $\lesssim 10^d$ , followed by a slower brightening over a month up to  $V_{\max} \approx 13.2$  ( $I_{\max} \approx 11.1$ ). The steady decline began after a short (JD 24558537–614) optical plateau, initially by  $\Delta V \sim 1$  ( $\Delta I \sim 0.6$ ) within about 180 days, and then, around JD 2458860 St 2-22 has come to a standstill at  $V \sim 14.5$  ( $I \sim 11.7$ ), with small amplitude fluctuations on timescales of  $\sim 300$  days.

While Tomov et al. (2017) needed support from spectroscopy in addition to photometry to prove the occurrence of the outburst, our light curve confirms the reality of the 2005 outburst. Tomov et al. (2017) also reported the outburst as relatively short,  $\lesssim 200^d$ . However, they did not observe the outburst onset, and they assumed an incorrect quiescent brightness of  $V = 15^m32$ . In fact, St 2-22 was not detected by ASAS before September 2004 which implies  $V \gtrsim 15$  (i.e. below the detection limit of ASAS) but then it remained invisible for  $\sim 5$  months (September – January) due to its position in the sky, and it was detected at  $V \sim 14.2$  just when it became visible again. Hence, it is very likely that the 2005 outburst occurred during the invisibility gap.

To search for any periodic changes, we analysed  $V$ -band light curve from the quiescent phase (JD 2454416–8283) using the discrete Fourier transform method in the *Period04* programme (Lenz & Berger 2005). We found two periods,  $P_1 = 891^d \pm 15$ , which could be attributed to the orbital cycle, and  $P_2 = 277^d \pm 1.7$ , which is most likely due to RG pulsation. However, there is no evidence for a much shorter period of  $51^d \pm 7$  reported by Tomov et al. (2017). The analysis of the  $I_C$ -band light curve confirmed the periods found in the  $V$ -band data within  $3\sigma$  error. Phased light curves are presented in Fig. A.1 (Appendix).

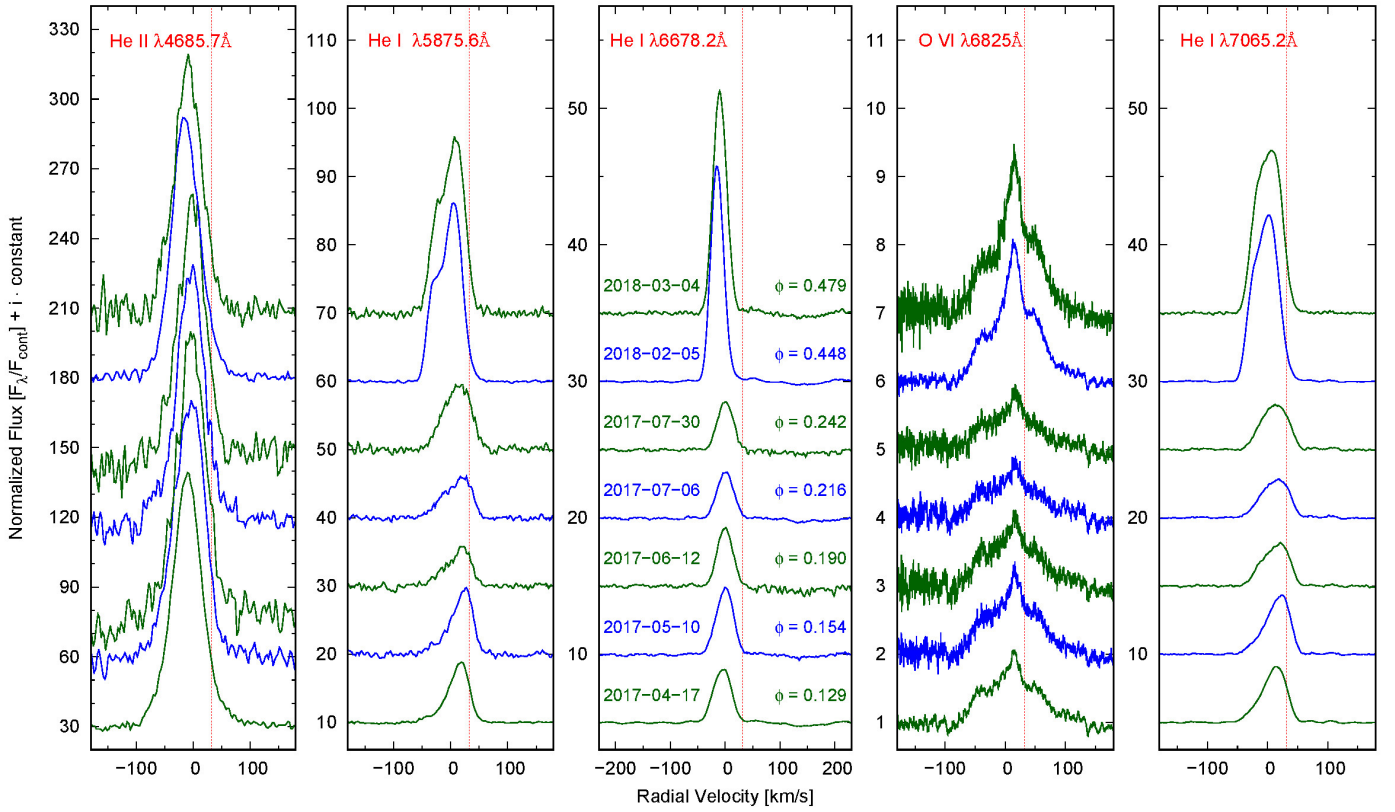


**Fig. 2.** Evolution of the He II ( $\lambda 4685.680 \text{ \AA}$ ) and He I ( $\lambda 5875.640 \text{ \AA}$ ,  $\lambda 6678.151 \text{ \AA}$ , and  $\lambda 7065.190 \text{ \AA}$ ) line profiles, and the Raman scattered O VI ( $\lambda 6825 \text{ \AA}$ ) line with the radial velocity scale corresponding to the parent O VI ( $\lambda 1032 \text{ \AA}$ ) line in the HRS/SALT spectra (Low-resolution mode:  $R \sim 14000$ ) collected during quiescence. The red dashed vertical lines mark the systemic velocity.

### 3.2. Spectral changes

HRS spectra cover all the phases of recent activity – the maximum, the standstill following the early decline, and the substantial part of the quiescent state (see Fig. 1). Quiescent spectra of St 2-22 are characteristic of most SySt, with prominent emission lines from H I, He I, He II, [O III] as well as high ionisation [Fe VII] lines and the Raman scattered O VI line (Fig. 2), and a strong red continuum with deep TiO absorption bands. The highest ionisation potential ( $IP_{\max}$ ) observed in the spectrum is given in Table 1 while the behaviour of the main emission line profiles is shown in Figs. A.2 and 2, and the equivalent widths are found in Table 2. The strength of H I and He I lines increases significantly in the spectra taken in 2018, preceding the outburst by almost a year. At the same time, the He II lines remain unchanged.

The outburst amplitude and timescales, as well as spectral changes, resemble those observed in other classical SySt (e.g. Z And, CI Cyg, and AX Per), the so-called Z And-type outbursts. In all epochs, in the observed members of the Balmer series, the broad emission is cut by a central absorption, blueshifted by  $\sim 30\text{--}40 \text{ km s}^{-1}$  with respect to the systemic velocity (Figs. A.2 and A.3). The lines become stronger during the outburst, and the absorption component seems to be broader, especially in the spectrum closest to the outburst maximum (February 15, 2019). All He I and He II lines completely or nearly disappear during the brightest phase of the outburst. The red giant absorption features (e.g. TiO bands) weaken, and at times (e.g. on July 1, 2020) almost completely disappear (Fig. 3). The spectra in the blue range are dominated by a hot continuum with absorption lines mostly from Ti II, Fe II, and Cr II which most closely resembles spectra of A–F supergiants. This so-called cF-shell

absorption system is believed to be linked to the hot companion and formed either in a thick accretion disc around the compact object (Mikołajewska & Kenyon 1992; Brandi et al. 2005) or in the stream of accreted matter (e.g. in AR Pav, RS Oph, & V3890 Sgr; Schild et al. 2001; Quiroga et al. 2002; Brandi et al. 2009; Mikołajewska et al. 2021).

The spectra taken in 2020, after the significant drop in optical brightness, reveal the reappearance of He II emission lines, while the blue continuum and cF-shell absorption lines are still present, although significantly weakened. However, the most remarkable change occurred in July 2020 when two satellite components with a velocity  $\sim \pm 1650 \text{ km s}^{-1}$  appeared in H $\alpha$  wings, which we attribute to a launch of bipolar jets. The jets were detected for the first time since their discovery during the 2005 outburst (Tomov et al. 2017), and they have been present in all subsequent spectra.

The FEROS spectra obtained in 2005 resemble the HRS spectra taken during the light curve standstill (2020 to 2021), and, in particular, the spectrum taken on February 1, 2005 is almost identical with the HRS spectrum on April 2, 2021 (almost exactly during a small secondary maximum). This suggests that both outbursts could have been similar and that the 2005 outburst had very likely started much earlier and reached a higher amplitude than reported by Tomov et al. (2017).

### 3.3. Spectroscopic orbits

All our spectra in the red region contain plenty of absorption lines from the atmosphere of the cool, red giant. We used the synthetic spectra from the BT-NextGen grid of the theoretical

**Table 2.** Journal of spectroscopic observations with information about time (UT, HJD, phase) and exposure times.

Date [UT] <sup>⋄</sup>	HJD <sup>⋄</sup>	Phase <sup>⋄</sup>	Exp. t.	He II λ4685.7	H <sub>β</sub>	[O III] λ5006.9	[Ca VII] λ5618.8	He I λ5875.6	[Fe VII] λ6087	H <sub>α</sub>	He I λ6678.2	O VI λ6825	He I λ7065.2
yyyy-mm-dd hh:mm:ss	-2450000		[sec.]	[Å]	[Å]	[Å]	[Å]	[Å]	[Å]	[Å]	[Å]	[Å]	[Å]
2005-02-01 06:16:51	3402.762	0.272	2×1800	9	32	11	0	9	0	230	6	0	7
2005-05-16 02:04:17	3506.591	0.385	2×1800	14	30	12	0	9	0	261	9	0	9
2017-04-17 19:48:06	7861.329	0.129	3×1200	98	74	5	3	8	4	202	4	13	5
2017-05-10 23:01:42	7884.464	0.154	3×400	191:	94:	3	4	9	4	265	4	14	5
2017-06-12 20:53:02	7917.373	0.190	3×400	nc	nc	0	2	5	5	256	4	11	4
2017-07-06 19:55:52	7941.333	0.216	3×400	nc	nc	nc	2	7	3	229	3	7	4
2017-07-30 18:31:00	7965.272	0.242	3×400	nc	nc	nc	3	14	3	246	3	8	4
2018-02-05 00:40:20	8154.528	0.448	3×1200	111	150	nc	4	26	4	549	10	19	16
2018-03-04 22:28:27	8182.438	0.479	3×600	nc	nc	0	5	33	5	587	12	24	16
2019-02-15 23:18:25	8530.472	0.858	2340	0	8	1	0	2	0	107	1	0	1
2019-03-30 02:00:56	8572.587	0.904	2200	0	9	0	0	0	0	113	0	0	0
2019-05-01 23:58:17	8605.503	0.940	2570	0	7	0	0	0	0	109	0	0	0
2019-06-08 21:06:40	8643.383	0.981	2950	0	13	0	0	3	0	175	2	0	2
2020-01-28 00:36:18	8876.525	0.235	2750	15	26	8	0	11	0	218	8	0	9
2020-05-10 22:47:55	8980.454	0.348	2750	14	32	10	0	11	0	228	8	0	10
2020-07-01 19:39:40	9032.322	0.404	2750	13	39	10	0	12	0	243	9	0	10
2021-02-04 00:35:29	9249.525	0.641	2900	10	32	7	0	7	0	189	7	0	7
2021-03-26 21:21:13	9300.393	0.697	2900	14	53	10	0	11	0	268	9	0	9
2021-05-02 18:17:17	9337.266	0.737	2600	10	43	9	0	9	0	245	7	0	9
2021-07-25 18:15:44	9421.262	0.828	2600	19	54	13	0	15	0	332	12	0	14

**Notes.** The right-hand columns separated by a vertical line show the measured equivalent widths (EWs) of emission lines. The errors are of the order of 1 Å. The sign 'nc' means that EW was not measured, although the line was visible because of a problem with estimating the continuum level due to low S/N. A colon designates the measurements that can be burdened with large uncertainty and are difficult to estimate. (⋄) Time at mid of exposure. (⋄) Phase according to the ephemeris:  $HJD_{T_0} = 2458661 + 918 \times E$  (Table 3).

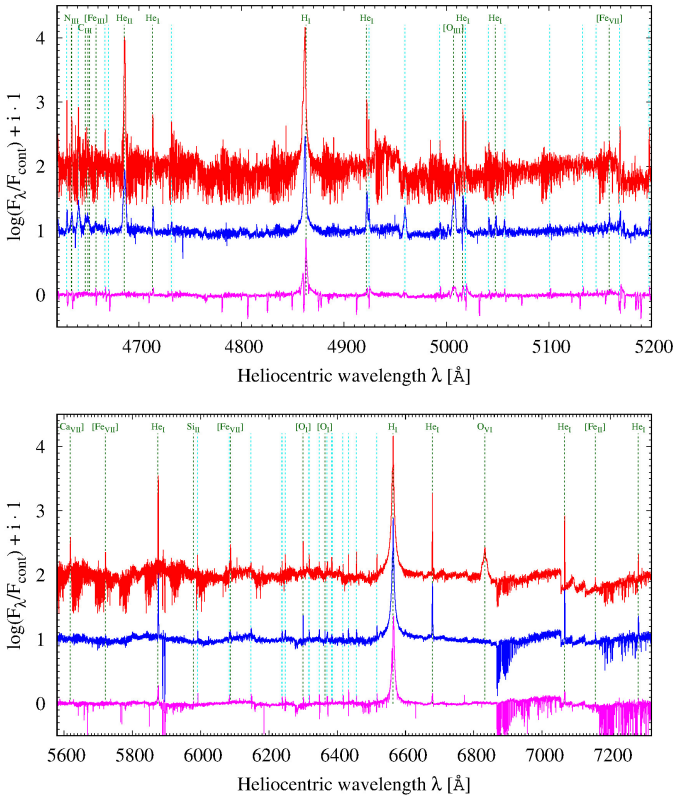


**Fig. 3.** Parts of blue (top), and red-arm (bottom), HRS/SALT spectra obtained close to the outburst maximum on February 15, 2019 (magenta), when the jets were first noticed on July 1, 2020 (blue), and during quiescence on February 5, 2018 (red). The laboratory wavelengths for identified emission lines are shown with green dashed lines labelled with the corresponding element. The position of the most frequent lines from singly ionised iron (Fe II) are shown with cyan dashed lines without labels for clarity.

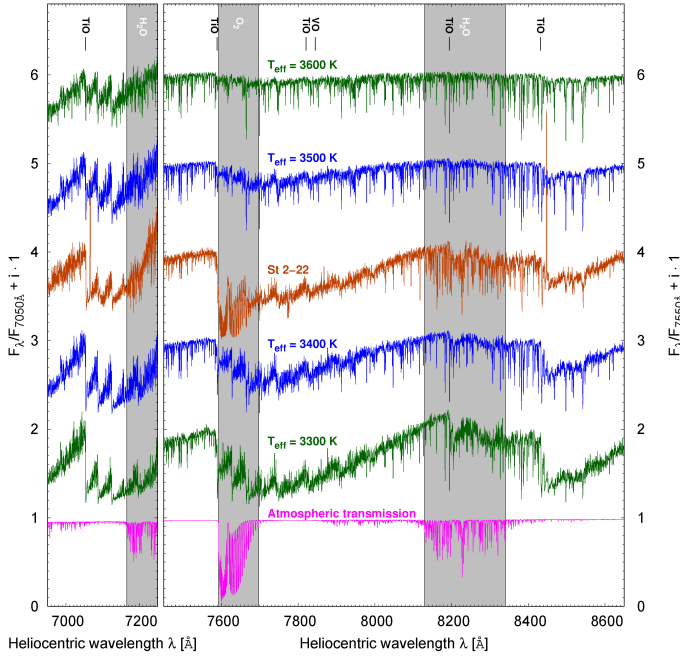
spectra of Allard et al. (2011)<sup>2</sup>, who used the solar abundances of Asplund et al. (2009), convolved with the appropriate profile, to meet the resolution of the observed spectra. The synthetic spectrum of an M5 III star ( $T_{\text{eff}} = 3400$  K,  $\log g = 0.5$ , and  $z = -0.25$ ) best fitted the observed quiescent spectra (see Fig. 4). To measure the radial velocities, our spectra were cross-correlated with the synthetic spectrum. To avoid the regions with emission lines or polluted by the telluric features from absorption of the Earth's atmosphere, the following masks were applied: 6110–6130, 6133–6147, 6597–6607, 6624–6656, 7069–7154, 7378–7513, 7899–8138, and 8670–8700 Å. The resulting velocities are given in Table 1 and plotted in Fig. 5.

Table A.1 lists more than 100 cF-shell absorption system lines, located in the range  $\sim 4200$ – $5200$  Å, which were identified in the Feros and HRS spectra taken from 2019 to 2021 and used to measure the radial velocities (Table 1). The radial velocities of these lines are in anti-phase with the red giant (Fig. 5), and we attribute them to the orbital motion of the WD.

Table 3 shows the orbital solutions. The obtained orbital period  $P_{\text{sp}} = 918 \pm 6^{\text{d}}$  is consistent within  $3\sigma$  errors with that from periodic analysis of the light curves. Due to its better precision, we adopt it as the final value. The best solution gives a significantly eccentric orbit (see Fig. 5), although the periastron longitude,  $\omega \sim 270^\circ$ , may indicate some geometrical effect tied to the line of sight as in AR Pav (Quiroga et al. 2002), FN Sgr (Brandi et al. 2005), and V3890 Sgr (Mikołajewska et al. 2021). However, in St 2-22 the same eccentric solution fits both radial velocity curves which suggests that the orbit is indeed eccentric. The semi-amplitudes of the radial velocity curves of both components indicate the mass ratio  $q = 3.50 \pm 0.53$ , the masses  $M_g \sin^3 i = 2.35 \pm 0.55 M_\odot$ , and  $M_{\text{WD}} \sin^3 i = 0.67 \pm 0.15 M_\odot$ , and the separation of the components  $a \sin i \sim 2.67$  AU. The lack of eclipses sets the upper limit for the orbit inclination,  $i \lesssim 70^\circ$ , whereas the lower limit,  $i \gtrsim 52^\circ$ , results from the fact that the WD cannot exceed the Chandrasekhar limit ( $M_{\text{WD}} \lesssim 1.4 M_\odot$ ). This in-

<sup>2</sup> <http://svo2.cab.inta-csic.es/theory/newov2/index.php>





**Fig. 4.** Average of three spectra of St 2-22 obtained during quiescence in June and July 2017, compared with the spectra from the grid BT-NextGen of the theoretical spectra (Allard et al. 2011,  $\log g = 0.5$  dex and  $T_{\text{eff}}$  in the range 3300–3600 K). The spectrum of St 2-22 most resembles the giant’s spectrum with  $T_{\text{eff}} = 3400$  K. The spectrum of the atmospheric transmission is shown at the bottom in magenta; it was not subtracted from the observed spectra. It was generated with the use of the TAPAS<sup>3</sup> service (Bertaux et al. 2014), adopting conditions similar to those during our observations in Sutherland.

icates a moderately massive WD,  $M_{\text{WD}} \geq 0.8 \pm 0.2 M_{\odot}$ . The red giant mass is then  $M_g \geq 2.8 \pm 0.7 M_{\odot}$ .

### 3.4. Red giant and distance

Gaia DR3 gives a parallax of  $\pi = 0.085 \pm 0.023$  mas (Gaia Collaboration 2021) for St 2-22, resulting in a value of a distance  $d = 6.88^{+1.01}_{-0.97}$  kpc (Bailer-Jones et al. 2021). The goodness-of-fit statistic parameter for this parallax is  $\text{gofAL} \approx 2.05$ , which means a good fit to the data, thus giving credibility to the measured distance. The 2MASS colours (Phillips 2007) and the mean quiescent  $V - I_c \sim 4.2$  (this paper) are consistent with M5 III ( $T_{\text{eff}} = 3400$  K; sec. 3.3) and the reddening  $E_{B-V} = 0.7 \pm 0.1$ , which agrees with the total Galactic extinction  $E_{B-V} < 0.80 \pm 0.04$  (Schlafly & Finkbeiner 2011) and is consistent with  $E_{B-V} = 0.81 \pm 0.10$  (Zamanov et al. 2021), as well as marginally consistent with  $E_{B-V} \sim 1 \pm 0.3$  estimated by Miko  ajewska et al. (1997). We adopt the distance  $d = 6.9$  kpc and  $E_{B-V} = 0.7$  for the rest of the paper.

The reddening-corrected  $K_0 = 7.97 \pm 0.05$  and  $(J - K)_0 = 1.20 \pm 0.09$  combined with the corresponding bolometric correction  $BC_K = 2.94 \pm 0.10$  (Bessel & Wood 1984) gives  $M_{\text{bol}} = -3.28 \pm 0.45$ , the luminosity  $L_g = 1631^{+835}_{-555} L_{\odot}$ , and the radius  $R_g = 117 \pm 20 R_{\odot}$ . The mass ratio,  $q \sim 3.5$ ,  $a \sin i \sim 2.7$  AU, and  $\sin i \lesssim 70^\circ$  (sec. 3.3), gives the Roche lobe radius  $R_{\text{RL}} = 0.5a \sim 306 R_{\odot}$  (Paczynski 1971, Eq. (4)) which indicates that the giant does not fill its tidal lobe even at the periastron ( $R_g/R_{\text{RL},p} \approx 0.5$ ).

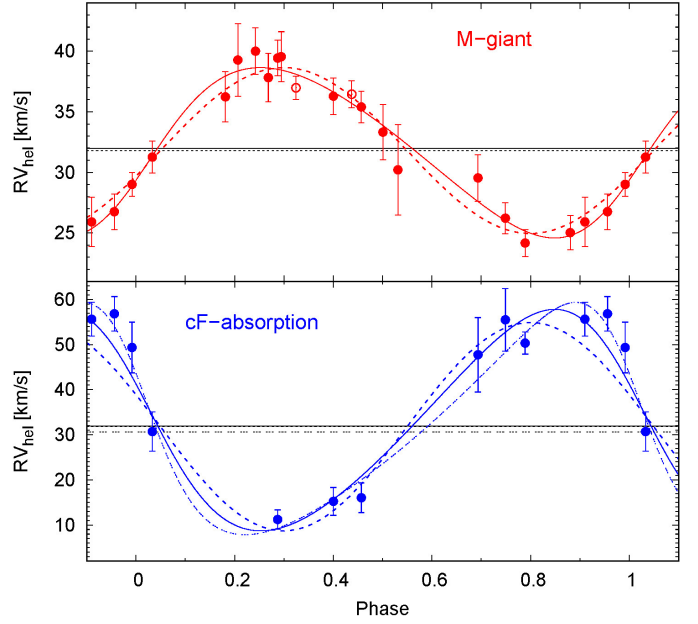


**Fig. 5.** Radial velocity curves of the cool (Top) and hot (Bottom) components folded with the period  $P_{\text{sp}} = 918^{\text{d}}$ . The values measured from SALT/HRS and FEROS data are shown with filled and open circles, respectively. Lines show synthetic radial velocity curves: for the case of the eccentric orbit (solid), circular orbit (dashed), and from the solution for  $RV_{\text{cF}}$  only (dot dashed). The corresponding horizontal lines represent the systemic velocities in these three cases.

Hut (1981) showed that in a binary with an eccentric orbit, the tidal force acts to synchronise the donor’s rotation with the orbital motion of the companion, and the equilibrium (called pseudo synchronisation) is reached for the rotational period,  $P_{\text{rot}}$ , lower than  $P_{\text{orb}}$  by an amount depending on the eccentricity. Using the orbital parameters for St 2-22 (Table 3), we estimated  $P_{\text{rot}}/P_{\text{orb}} = 0.86 \pm 0.09$  (Hut 1981, Eq. (42)) which combined with the RG rotational velocity  $v \sin i = 9.8 \pm 1.5 \text{ km s}^{-1}$  (Zamanov et al. 2008) gives the RG radius  $R_g = 153 \pm 40 R_{\odot}$ , in good agreement with that derived above.

The luminosity and effective temperature ( $\log T_{\text{eff}} = 3.53$ ,  $\log L_g = 3.21 \pm 0.20$ ) locate the giant on the HR diagram between the evolutionary tracks of 1.6 and 2.5  $M_{\odot}$  (e.g. Hurley et al. 2000), which more or less agree with our dynamical mass estimate (sec. 3.3). The systemic velocity  $\gamma = 32.58 \text{ km s}^{-1}$  and proper motions  $\mu_{\alpha} \cos \delta = -5.713 \pm 0.018 \text{ mas yr}^{-1}$  and  $\mu_{\delta} = 1.085 \pm 0.022 \text{ mas yr}^{-1}$  imply the following Galactic velocities:  $U = -136$ ,  $V = -138$ , and  $W = -16.3 \text{ km s}^{-1}$  which via confrontation with the Toomre diagram (see, e.g. Feltzing et al. 2003, – fig. 1) suggest that St 2-22 may belong to the extended thick-disc population, despite being placed relatively close to the Galactic plane  $z = 0.46 \pm 0.08 \text{ kpc}$  ( $b = 3.87^\circ$ ).

### 3.5. Hot component activity and jet evolution

The optical magnitudes recorded for St 2-22 was  $\langle V \rangle_{\text{hot}} \approx 13.25$  during the optical plateau (JD 2458537–614), which after correcting for the RG contribution ( $V_g \approx 16.2$ ) corresponds to  $V_{\text{hot}} \approx 13.3$ . Assuming that most of the hot component continuum emission is shifted to the optical (a lower limit to luminosity if not), and that during outburst  $m_{\text{bol}} \approx V_{\text{hot}}$ , we estimate the reddening corrected  $m_{\text{bol}} \approx 11.1$ , and the absolute bolometric magnitude  $M_{\text{bol}} \approx -3.1$ , which corresponds to  $L_{\text{hot}} \approx 1380 L_{\odot}$ .

<sup>3</sup> <http://cds-espri.ipsl.fr/tapas/>

**Table 3.** Orbital solutions for St 2-22.

$P_{\text{orb}}$ [day]	$V_{\gamma}$ [km s <sup>-1</sup> ]	$K_g$ [km s <sup>-1</sup> ]	$K_h$ [km s <sup>-1</sup> ]	$q$ [ $M_g M_h^{-1}$ ]	$e$	$\omega$ [deg]	$T_0^a$ [JD-2450000]	$T_{\text{ic}}^b$	$f(m)$ [ $M_{\odot}$ ]	$a \sin i$ [AU]
918.0 ± 6.0	31.98 ± 0.30	7.03 ± 0.45	24.6 ± 1.9	3.50 ± 0.53	0.16 ± 0.07	251 ± 22	8613 ± 52	8661	0.0331 ± 0.0066	2.67 ± 0.55
918.0 <sup>c</sup>	30.66 ± 1.74	—	25.8 ± 2.8	—	0.29 ± 0.09	67 ± 27	8613 ± 49	—	—	—
922.1 ± 6.4	31.80 ± 0.34	6.85 ± 0.44	23.1 ± 2.4	3.37 ± 0.61	0	—	—	8658.8 ± 10.4	0.0307 ± 0.0062	2.54 ± 0.60

**Notes.** The errors are  $1\sigma$  values. <sup>(a)</sup>  $T_0$  is a time of the periastron passage for the eccentric orbit. <sup>(b)</sup>  $T_{\text{ic}}$  is a time of inferior conjunction. <sup>(c)</sup> Additional solution for RV<sub>cf</sub> only, adopting an orbital period from the eccentric solution when velocities of both components were used.

**Table 4.** Radial velocities (RV) of the jets, FWHM values, and equivalent widths (EW) measured in the HRS and FEROS spectra.

HJD -2450000	Phase <sup>a</sup>	$V_{\gamma}^-$ [km s <sup>-1</sup> ]	FWHM <sup>-</sup> [km s <sup>-1</sup> ]	EW <sub>λ</sub> <sup>-</sup> [Å]	$V_{\gamma}^+$ [km s <sup>-1</sup> ]	FWHM <sup>+</sup> [km s <sup>-1</sup> ]	EW <sub>λ</sub> <sup>+</sup> [Å]	$V_{\gamma}^b$ [km s <sup>-1</sup> ]	VC <sub>J</sub> <sup>c</sup> [km s <sup>-1</sup> ]	EW <sub>λ</sub> <sup>-</sup> /EW <sub>λ</sub> <sup>+</sup>	$V$ [mag]	$I_c$ [mag]
3402.76	0.272	-1578	380	1.4	1534	338	1.3	1556	-22	1.1	14.15	—
3506.59	0.386	—	—	—	1752	332	1.0	1752	—	—	14.37	—
9032.32	0.404	-1642	297	1.1	1688	234	0.7	1665	23	1.6	14.76	11.78
9249.52	0.642	-1464	164	0.8	1558	237	0.5	1511	47	1.7	14.36	11.62
9300.39	0.696	-1604	223	1.0	1789	201	0.5	1697	92.5	1.8	14.54	11.73
9337.27	0.736	-1604	339	2.0	1795	324	1.1	1700	95.5	1.8	14.48	11.71
9421.26	0.828	-1588	316	1.5	1692	268	0.9	1640	52	1.7	14.84	11.88

**Notes.** The  $1\sigma$  uncertainties are of the order of 10–20 km s<sup>-1</sup> for RV and FWHM, and 0.1–0.2 for EW. <sup>(a)</sup> Phase according to the ephemeris:  $HJD_{T_0} = 2458661 + 918 \times E$  (Table 3). <sup>(b)</sup>  $V_{\gamma} = (|V_{\gamma}^-| + |V_{\gamma}^+|)/2$ . <sup>(c)</sup>  $VC_J = (V_{\gamma}^- + |V_{\gamma}^+|)/2$ .

Similarly, we estimate the luminosity of the F-type component,  $L_{\text{hot}} \sim 300\text{--}400 L_{\odot}$ , during the standstill from 2020 to 2021 and in 2005, respectively. In addition, to the F-type features, the spectra display very strong H $\alpha$ , He I, and He II emission lines. Unfortunately, the SALT spectra are not flux-calibrated, thus we cannot estimate the emission line fluxes and the corresponding temperature and luminosity of the ionising source. The FEROS spectra have relative flux-calibration, and we applied an absolute flux scale to the observed  $V$  mag (Table 4) such that convolution of the spectrum with the Johnson  $V$  filter agrees with the  $V$  mag. The emission line fluxes measured on the calibrated FEROS spectra are  $F(H\beta) = 7.7$  and  $7.4 \times 10^{-14}$  erg s<sup>-1</sup> cm<sup>-2</sup>,  $F(\text{He I } 5876) = 9.3$  and  $8.3 \times 10^{-14}$  erg s<sup>-1</sup> cm<sup>-2</sup>, and  $F(\text{He II } 4686) = 1.2$  and  $2.0 \times 10^{-14}$  erg s<sup>-1</sup> cm<sup>-2</sup> on February 1 and May 5, 2005, respectively. These values are significantly different from those reported by Tomov et al. (2017) (table 1): For example, the reddened (using their  $E_{B-V} = 1$ ) values of  $F(H\beta) = 1.0$  and  $2.8 \times 10^{-13}$  erg s<sup>-1</sup> cm<sup>-2</sup> from February 1 and May 5, 2005, respectively, are larger than ours, and, moreover, the fluxes measured in May are  $\sim 3$  times larger than those in February, whereas both the observed  $V$  mag and the EWs (Tables 2 and 4) are practically identical. Apparently, there is something wrong with the absolute flux calibration of the FEROS spectra in Tomov et al. (2017). Assuming a blackbody spectrum and case B recombination, the fluxes of H $\beta$ , He I 5876, and He II 4686 lines require  $T_h \sim 100$  kK (also indicated by the presence of weak [Fe VII] emission lines in the best-exposed spectra), and luminosity (within a factor of 2),  $L_h \sim 200 L_{\odot}$  (see, e.g. Merc et al. 2020). The estimated luminosity is similar to the quiescent  $L_h \approx 220 L_{\odot}$  resulting from the emission line fluxes published by Mikołajewska et al. (1997) corrected for the reddening and distance adopted in this study (Sec. 3.4), although the line ratios indicate a higher temperature,  $T_h \sim 140$  kK. Based on the lack of Raman scattered lines in this spectrum, Tomov et al. (2017) suggested that this spectrum was obtained during another missed outburst. However, the visual magnitude,  $V \approx 15.5 \pm 0.3$ , that we derived from this spectrum is more or less consistent with quiescent magnitudes (Figs 1 and A.1), and the lack of the Raman

O VI and [Fe VII] lines is probably due to insufficient sensitivity to detect these relatively faint lines of this observation.

The simultaneous presence of the F-type component and the much hotter ionising source points to a double-temperature structure of the active hot component that can be associated with an accretion disc. The F-type shell spectrum would be then formed in the optically thick disc seen nearly edge-on ( $i \lesssim 70^\circ$ ), while the hot radiation produced in a boundary layer and/or in the innermost disc regions would photoionise low density material above and below the disc and give rise to strong emission lines. A similar interpretation was proposed for other active SySt which simultaneously show an A/F-type shell spectrum and high ionisation emission lines (e.g. Kenyon & Webbink 1984; Quiroga et al. 2002; Mikołajewska et al. 2021). The luminosities estimated for both components agree within a factor of two which supports such an interpretation. Finally, the presence of an accretion disc is also compatible with the jet production.

Figure 6 shows the evolution of the jet components in the H $\alpha$  line profile. The jets are clearly visible as two satellite emission components at velocity  $V_{\gamma} \sim \pm 1650$  km s<sup>-1</sup> in the spectrum acquired in July 2020 (JD 2459032), while they were absent in that taken in May (JD 2458980). This indicates that the jets were launched somewhere between May and July, shortly after St 2-22 reached a standstill in the optical light curve. These additional components are present in all subsequent spectra.

Table 4 presents radial velocities (measured by fitting Gaussian profiles) of both – approaching ( $V_{\gamma}^-$ ) and receding ( $V_{\gamma}^+$ ) – jets together with the values of full widths at half maximum (FWHM), equivalent width (EW), and other characteristics. The outflow velocities, FWHMs, and EWs vary with time although there are no obvious trends. The approaching component is always stronger than the receding one with  $EW_{\lambda}^-/EW_{\lambda}^+ \sim 2$  from 2020–2021. The slowest jets were observed on JD 2459249, and their FWHM and EW are the lowest there as well. On the contrary, during the 2005 outburst, the slowest jets were observed on February 1 (JD 2453402) when their FWHM and EW were at their highest values. However, in any case, the departures of the jet radial velocity  $V_{\gamma}$ , and FWHM from their average values,  $\langle V_{\gamma} \rangle = 1647 \pm 48$  km s<sup>-1</sup> and  $\langle \text{FWHM} \rangle = 279 \pm 21$  km s<sup>-1</sup>, are less than  $\sim 10\%$ . Assuming that the jets are launched per-

pendicularly to the disc and orbital plane, the jet opening angle,  $\phi$ , is related to the observed jet width ( $\Delta v$ ) and radial velocity,  $\Delta v = 2 V_J \sin \phi/2$ , (e.g. Solf 1987). Using the average FWHM and  $V_J$  values, we estimate  $\phi \sim 10^\circ$ . The total width of the jet component is a factor of  $\sim 2$  larger which may suggest a somewhat larger cone. However, in any case, the degree of collimation is quite high. The jet centre velocity,  $V_{CJ}$ , seems to follow the WD radial velocities, but with a higher amplitude (Fig. A.5); more observations are, however, necessary to confirm this behaviour.

The general picture for the majority of jets is that the outflow velocity corresponds to the escape velocity at their origin (Livio 1998). Hence, the maximum expansion velocity is set by the WD escape velocity since no ejection can originate under its surface. Assuming the jet expansion perpendicular to the orbital plane, the expansion velocity is  $2675 \text{ km s}^{-1} \lesssim V_{\text{exp}} = V_J \cos^{-1} i \lesssim 4816 \text{ km s}^{-1}$  for  $52^\circ \lesssim i \lesssim 70^\circ$  (Sec. 3.3). The WD escape velocity,  $v_{\text{esc}}$ , increases with WD mass and by the same token with decreasing inclination ( $M_{\text{WD}} \approx 0.67 \sin^{-3} i M_\odot$ ), in particular,  $v_{\text{esc}} \approx 5500 \pm 1500 \text{ km s}^{-1}$  for  $M_{\text{WD}} \approx 0.8 \pm 0.2 M_\odot$  (Sec. 3.3). Hence, the binary inclination should be close to its upper limit,  $i \sim 70^\circ$  if the jets are launched near the WD.

#### 4. Epilogue

Based on high-resolution spectroscopy combined with 16 years of optical photometry, we have revealed the nature of the S-type symbiotic binary St 2-22 and derived physical parameters of the system components. Our double-line spectroscopic orbits indicate the orbital period  $P_{\text{orb}} = 918^{\text{d}}$ , the mass ratio  $q = M_g/M_{\text{WD}} = 3.50 \pm 0.5$ , and significant eccentricity  $e = 0.16 \pm 0.07$ . The most likely orbital solution for the component masses are  $M_{\text{WD}} \approx 0.8 \pm 0.2 M_\odot$  and  $M_g \approx 2.8 \pm 0.7 M_\odot$ , whereas the orbit inclination is  $\sim 70^\circ$ .

St 2-22 shows outbursts with amplitudes in the range from 2–3 mag, which seem to recur with a timescale of a dozen years. In the quiescence, the changes  $\Delta V \approx 0^{\text{m}}.5$  are observed with the period  $P = 277^{\text{d}} \pm 1.7$ . The outburst behaviour of St 2-22 resembles that of the classical symbiotic binary Z And, and its binary parameters very similar to those of Z And (masses, temperatures, luminosities, etc.; Mikołajewska & Kenyon 1992) makes St 2-22 almost a twin in a slightly wider orbit. In both systems, we observed the ejection of strongly collimated jets during the late outburst phase. The jet behaviour in St 2-22, overall, resembles that in Z And where gradual changes within  $200\text{--}300 \text{ km s}^{-1}$  were observed on a time scale of several months (Skopal et al. 2009), with the difference that the jets of St 2-22 were undetectable in H $\beta$  (probably due to the sensitivity of our spectra being too low); additionally, in St 2-22, after their first appearance in July 2020, we observed first deceleration and then acceleration of the jets. The phenomenon is still ongoing and our monitoring is continued. We also encourage high-resolution ( $R \gtrsim 15000$ ) spectroscopic monitoring to document the outburst and jet evolution well.

**Acknowledgements.** We dedicate this work to the memory of the wonderful man and friend, Toma Tomov, who sadly passed away in 2019. The present work is a continuation of the research he initiated and CG had the honour to participate. This research has been partly financed by the Polish National Science Centre (NCN) grants OPUS 2017/27/B/ST9/01940, MAESTRO 2015/18/A/ST9/00746, and SONATA No. DEC-2015/19/D/ST9/02974. KI was supported by STFC [ST/T000244/1]. The paper is based on spectroscopic observations made with the Southern African Large Telescope (SALT) under programmes: 2017-1-SCI-046 and 2017-2-SCI-044 (PI: T. Tomov), and 2018-2-SCI-021 and 2019-1-MLT-

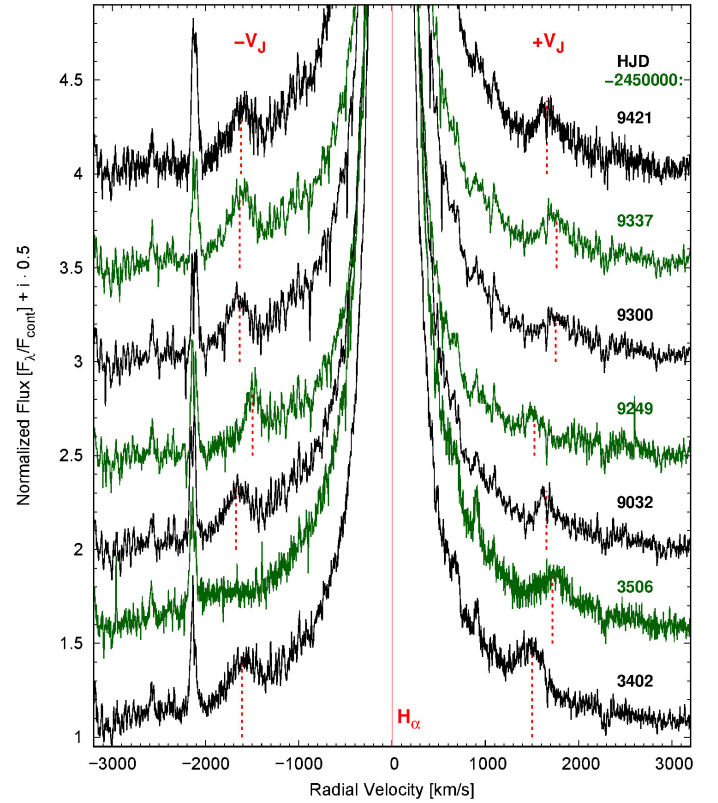


**Fig. 6.** Evolution of H $\alpha$  line profile in the high-resolution spectra (HRS and FEROS) of St 2-22 with visible emission components from collimated jets on its wings. The measured positions of their centres (Table 4) after correction on  $V_y$  are shown with red dashed lines.

008 (PI: C. Gałań). Polish participation in SALT is funded by grant No. MNiSW DIR/WK/2016/07.

#### References

- Allard, F., Homeier, D., & Freytag, B. 2011, ASP Conf. Ser., 448, 91
- Allen, D. A. 1984, PASA, 5, 369
- Asplund, M., Grevesse, N., Sauval, A., & Scott, P. 2009, ARA&A, 47, 481
- Bailer-Jones, C. A. L., Rybizki, J., Fouesneau, M., et al. 2021, AJ, 161, 147
- Bertaux, J. L., Lallement, R., Ferron, S., et al. 2014, A&A, 564, A46
- Bessell, M. S., & Wood, P. R. 1984, PASP, 96, 24
- Brandi, E., Mikołajewska, J., Quiroga, C., et al. 2005, A&A, 440, 239
- Brandi, E., Quiroga, C., Mikołajewska, J., et al. 2009, A&A, 497, 815
- Feltzing, S., Bensby, T., & Lundström, I. 2003, A&A, 397, 1
- Gaia Collaboration: Brown, A., Vallenari, A., Prusti, T., et al. 2021, A&A, 649, 1
- García, L. G., Brandi, E., Ferrer, O., Quiroga, C. 2003, ASP Conf. Ser., 303, 458
- Hurley, J. R., Pols, O. R., & Tout, C. A. 2000, MNRAS, 315, 543
- Hut, P. 1981, A&A, 99, 126
- Kenyon, S. J. & Webbink, R. F. 1984, ApJ, 279, 252
- Kniazev, A. Y., 2016, Doc. number: HRS0000006, Version: 1.0; Technical report, MIDAS automatic pipeline for HRS data. Southern African Large Telescope
- Kniazev, A. Y., Gvaramadze, V. V., Berdnikov, L. N. 2017, ASPCS, 510, 48
- Kochanek, C. S., Shappee, B. J., Stanek, K. Z., et al. 2017, PASP, 129, 104502
- Lenz, P., & Breger, M. 2005, Communications in Asteroseismology, 146, 5
- Livio, M. 1998, ASP Conf. Ser. 137, 264
- Merc, J., Mikołajewska, J., Gromadzki, M., Gałań, C., Ilkiewicz, K., et al. 2020, A&A 644, A49
- Mikołajewska, J., & Kenyon, S. J. 1992, AJ, 103, 579
- Mikołajewska, J., Acker, A., Stenholm, B. 1997, A&A, 327, 191
- Mikołajewska, J., Ilkiewicz, K., Gałań, C., et al. 2021, MNRAS, 504, 2122
- Mürset, U., & Schmid, H. M. 1999, A&AS, 137, 473
- Paczynski, B. 1971, ARA&A 9, 183
- Phillips, J. P., 2007, MNRAS, 376, 1120
- Pojmański, G., 1997, Acta Astron., 47, 467
- Quiroga, C., Mikołajewska, J., Brandi, E., et al. 2002, A&A, 387, 139
- Sanduleak, N. 1976, Publications of the Warner and Swasey Observatory, 2, 55

- Shappee, B. J., Prieto, J. L., Grupe, D., et al. 2014, *ApJ*, 788, 48  
Schild, H., Dumm, T., Mürset, U., et al. 2001, *A&A*, 366, 972  
Schlafly, E. F., & Finkbeiner, D. P. 2011, *ApJ*, 737, 103  
Shafter, A. W. 1983, *ApJ*, 267, 222  
Skopal, A., Pribulla, T., Budaj, J., et al. 2009, *ApJ*, 690, 1222  
Solf, J. 1987, *A&A*, 180, 207  
Tomov, T., Zamanov, R., Gałan, C., & Pietrukowicz, P. 2017, *AcA*, 67, 225  
Van Winckel, H., Duerbeck, H. W., Schwarz H. E. 1993, *A&AS*, 102, 401  
Zamanov, R. K., et al. 2008, *MNRAS*, 390, 377  
Zamanov, R. K., Marchev, V. D., & Stoyanov, K. A. 2021, *Bulg. Astron. J.*, 34, 3



## Appendix A: Supplementary tables and figures

**Table A.1.** Blue cF-type absorption lines (from Ca I, Sc II, Ti II, Cr II, Fe I, Fe II, Y II, and Zr II) that were identified in the high-resolution spectra collected during outbursts and used to measure the radial velocities associated with the hot component.

Element $\lambda_{\text{lab}}$ (Å)	Element $\lambda_{\text{lab}}$ (Å)	Element $\lambda_{\text{lab}}$ (Å)
Cr II 4242.364	Ti II 4394.051	Fe II 4534.168
Sc II 4246.822	Ti II 4395.031	Fe II 4541.524
Fe I 4271.154	Ti II 4395.839	Fe II 4549.474
Fe I 4271.761	Ti II 4399.765	Ti II 4549.622
Fe II 4273.320	Sc II 4400.389	Fe II 4555.893
Fe II 4273.325	Fe I 4404.750	Cr II 4558.650
Cr II 4275.567	Ti II 4407.672	Ti II 4563.757
Fe I 4282.403	Fe I 4407.709	Ti II 4571.971
Ti II 4287.873	Ti II 4409.235	Fe II 4576.340
Fe II 4296.572	Ti II 4409.516	Fe II 4582.835
Ti II 4300.042	Ti II 4411.072	Fe II 4583.837
Ti II 4301.914	Ti II 4411.929	Cr II 4588.199
Sc II 4305.714	Ti II 4418.330	Ti II 4589.958
Ti II 4307.863	Ti II 4421.938	Cr II 4592.049
Fe I 4307.902	Fe I 4422.568	Fe II 4629.339
Ti II 4312.860	Y II 4422.585	Cr II 4634.070
Sc II 4314.083	Ca I 4434.957	Ti II 4763.883
Fe II 4314.310	Ca I 4435.679	Ti II 4764.526
Ti II 4314.971	Ti II 4441.729	Ti II 4779.985
Fe I 4315.085	Fe I 4442.339	Ti II 4798.521
Sc II 4320.732	Ti II 4443.794	Ti II 4805.085
Ti II 4320.950	Ti II 4444.555	Cr II 4812.337
Sc II 4324.996	Ti II 4450.482	Cr II 4824.127
Fe I 4325.762	Ca I 4454.779	Cr II 4836.229
Ti II 4330.237	Fe I 4461.653	Cr II 4848.235
Ti II 4330.240	Ti II 4464.449	Ti II 4874.010
Ti II 4330.695	Ti II 4468.507	Cr II 4876.399
Ti II 4344.281	Fe II 4489.183	Cr II 4876.410
Sc II 4354.598	Fe II 4491.405	Y II 4900.119
Ti II 4367.652	Ti II 4501.270	Ti II 4911.195
Sc II 4374.457	Fe II 4508.288	Fe II 4923.927
Ti II 4374.816	Fe II 4515.339	Fe II 5018.440
Y II 4374.933	Ti II 4518.327	Sc II 5031.021
Zr II 4379.742	Fe II 4520.224	Ti II 5072.287
Sc II 4384.814	Fe II 4522.634	Ti II 5185.902
Fe II 4385.387	Ti II 4529.480	Ti II 5188.687
Ti II 4391.025	Ti II 4533.960	

**Table A.2.** Emission lines identified in the HRS/SALT blue- and red-arm spectra of St 2-22.

Line	Line	Line
H $\delta$ ( $\lambda$ 4101.7 Å)	Fe II ( $\lambda$ 5040.8 Å)	Fe II ( $\lambda$ 6370.3 Å)
Fe II ( $\lambda$ 4233.2 Å)	He I ( $\lambda$ 5047.7 Å)	Fe II ( $\lambda$ 6383.7 Å)
H $\gamma$ ( $\lambda$ 4341.3 Å)	Fe II ( $\lambda$ 5057.0 Å)	Fe II ( $\lambda$ 6385.5 Å)
[O III] ( $\lambda$ 4363.8 Å)	Fe II ( $\lambda$ 5100.7 Å)	Fe II ( $\lambda$ 6416.9 Å)
He I ( $\lambda$ 4387.9 Å)	Fe II ( $\lambda$ 5132.6 Å)	Fe II ( $\lambda$ 6432.7 Å)
He I ( $\lambda$ 4471.5 Å)	Fe II ( $\lambda$ 5145.8 Å)	Fe II ( $\lambda$ 6456.4 Å)
Mg II ( $\lambda$ 4481.2 Å)	[Fe VII] ( $\lambda$ 5158.9 Å)	Fe II ( $\lambda$ 6516.1 Å)
Fe II ( $\lambda$ 4491.4 Å)	Fe II ( $\lambda$ 5169.0 Å)	H $\alpha$ ( $\lambda$ 6562.8 Å)
Fe II ( $\lambda$ 4508.3 Å)	Fe II ( $\lambda$ 5197.6 Å)	He I ( $\lambda$ 6678.2 Å)
Fe II ( $\lambda$ 4515.3 Å)	Fe II ( $\lambda$ 5234.6 Å)	O VI ( $\lambda$ 6832 Å)
Fe II ( $\lambda$ 4522.6 Å)	Fe II ( $\lambda$ 5254.4 Å)	He I ( $\lambda$ 7065.2 Å)
He II ( $\lambda$ 4542 Å)	[Fe II] ( $\lambda$ 5262.3 Å)	[Fe II] ( $\lambda$ 7155.2 Å)
Fe II ( $\lambda$ 4555.9 Å)	Fe II ( $\lambda$ 5264.8 Å)	He I ( $\lambda$ 7281.3 Å)
Mg I ( $\lambda$ 4571.1 Å)	Fe II ( $\lambda$ 5276.0 Å)	Fe II ( $\lambda$ 7462.4 Å)
Fe II ( $\lambda$ 4576.3 Å)	Fe II ( $\lambda$ 5284.1 Å)	Fe II ( $\lambda$ 7516.2 Å)
Fe II ( $\lambda$ 4583.8 Å)	Fe II ( $\lambda$ 5316.6 Å)	Fe II ( $\lambda$ 7711.4 Å)
Fe II ( $\lambda$ 4620.5 Å)	Fe II ( $\lambda$ 5363.0 Å)	Fe II ( $\lambda$ 7866.6 Å)
Fe II ( $\lambda$ 4629.3 Å)	He II ( $\lambda$ 5411.5 Å)	Fe II ( $\lambda$ 7877.0 Å)
N III ( $\lambda$ 4630.6 Å)♦	Fe II ( $\lambda$ 5414.9 Å)	Mg II ( $\lambda$ 7896.4 Å)
N III ( $\lambda$ 4642.0 Å)♦	Fe II ( $\lambda$ 5425.3 Å)	H I ( $\lambda$ 8333.8 Å)
C III ( $\lambda$ 4647.4 Å)♦	Fe II ( $\lambda$ 5534.9 Å)	H I ( $\lambda$ 8345.5 Å)
C III ( $\lambda$ 4652.0 Å)♦	[O I] ( $\lambda$ 5577.3 Å)	H I ( $\lambda$ 8359.0 Å)
Fe II ( $\lambda$ 4640.8 Å)	[Ca VII] ( $\lambda$ 5618.8 Å)	H I ( $\lambda$ 8374.5 Å)
[Fe III] ( $\lambda$ 4658.1 Å)	[Fe VII] ( $\lambda$ 5720.7 Å)	H I ( $\lambda$ 8392.4 Å)
Fe II ( $\lambda$ 4666.7 Å)	He I ( $\lambda$ 5875.6 Å)	H I ( $\lambda$ 8413.3 Å)
Fe II ( $\lambda$ 4670.2 Å)	Si II ( $\lambda$ 5978.9 Å)	H I ( $\lambda$ 8438.0 Å)
He II ( $\lambda$ 4685.7 Å)	Fe II ( $\lambda$ 5991.4 Å)	O I ( $\lambda$ 8446.4 Å)
He I ( $\lambda$ 4713.2 Å)	Fe II ( $\lambda$ 6084.1 Å)	H I ( $\lambda$ 8467.3 Å)
Fe II ( $\lambda$ 4731.4 Å)	[Fe VII] ( $\lambda$ 6087.0 Å)	Ca II ( $\lambda$ 8498.0 Å)
H $\beta$ ( $\lambda$ 4862.9 Å)	Fe II ( $\lambda$ 6147.7 Å)	H I ( $\lambda$ 8502.5 Å)
He I ( $\lambda$ 4921.9 Å)	Fe II ( $\lambda$ 6238.4 Å)	Ca II ( $\lambda$ 8542.1 Å)
Fe II ( $\lambda$ 4924.3 Å)	Fe II ( $\lambda$ 6247.6 Å)	H I ( $\lambda$ 8545.4 Å)
Fe II ( $\lambda$ 4959.6 Å)	[O I] ( $\lambda$ 6300.3 Å)	H I ( $\lambda$ 8598.4 Å)
Fe II ( $\lambda$ 4993.4 Å)	He II ( $\lambda$ 6311 Å)	Ca II ( $\lambda$ 8662.1 Å)
[O III] ( $\lambda$ 5006.8 Å)	Fe II ( $\lambda$ 6317.4 Å)	H I ( $\lambda$ 8665.0 Å)
He I ( $\lambda$ 5015.7 Å)	Fe II ( $\lambda$ 6347.6 Å)	H I ( $\lambda$ 8750.5 Å)
Fe II ( $\lambda$ 5018.4 Å)	[O I] ( $\lambda$ 6363.8 Å)	

**Notes.** (♦) These are bands composed of several lines. The initial and the ending wavelengths are only given.

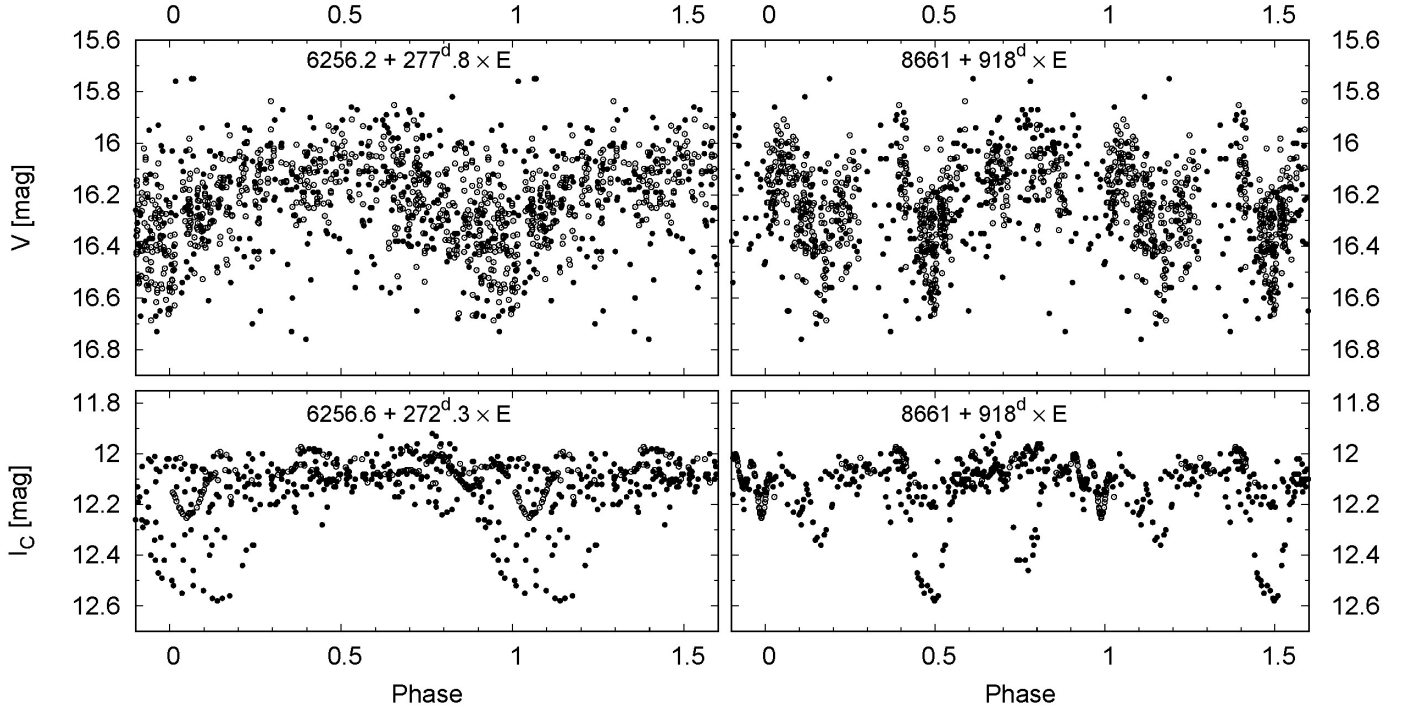


**Fig. A.1.** *V* (Top) and *I* (Bottom) light curves folded with the shorter (Left) and the longer (Right) periods, respectively, with the adopted ephemerides given at the top of each plot. Filled and open circles correspond to the *Kleinkaroo* and *ASAS-SN/OGLE* data, respectively.

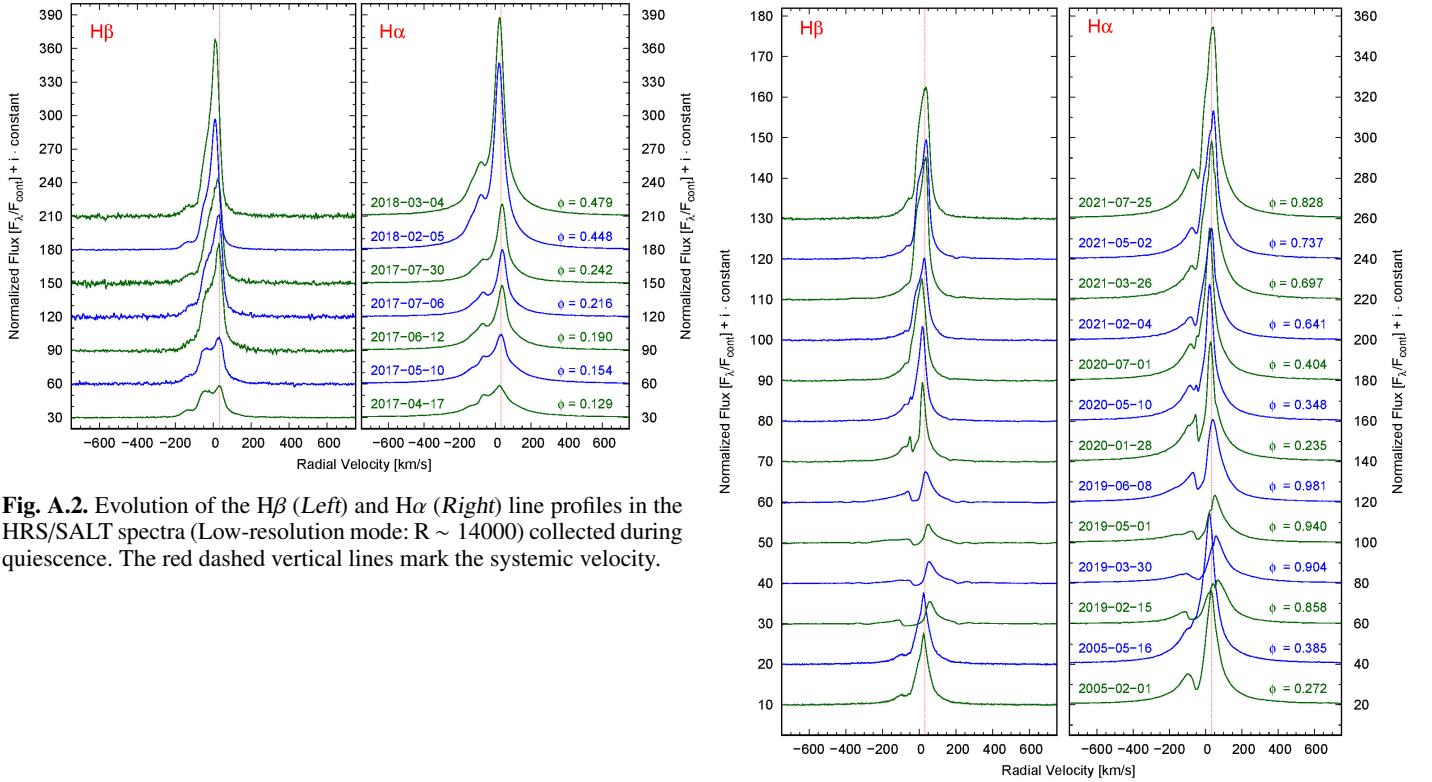


**Fig. A.2.** Evolution of the H $\beta$  (Left) and H $\alpha$  (Right) line profiles in the HRS/SALT spectra (Low-resolution mode:  $R \sim 14000$ ) collected during quiescence. The red dashed vertical lines mark the systemic velocity.

**Fig. A.3.** Evolution of the H $\beta$  (Left) and H $\alpha$  (Right) line profiles during the last outburst in the HRS/SALT spectra (medium-resolution mode:  $R \sim 40000$ ) and two FEROS spectra taken during the previous outburst in 2005. The red dashed vertical lines mark the systemic velocity.

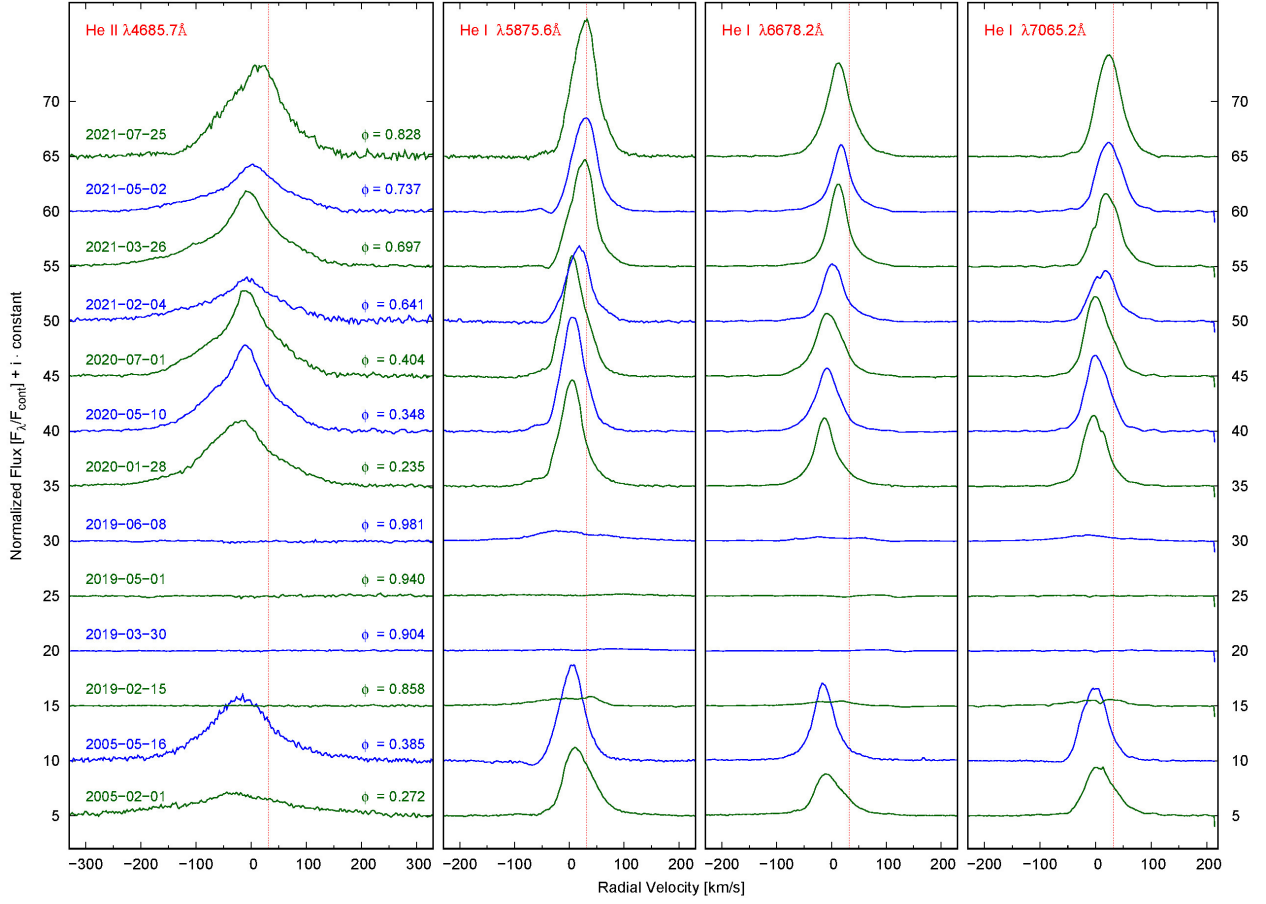


**Fig. A.4.** Evolution of the He II ( $\lambda 4685.680 \text{ \AA}$ ) and He I ( $\lambda 5875.640 \text{ \AA}$ ,  $\lambda 6678.151 \text{ \AA}$ , and  $\lambda 7065.190 \text{ \AA}$ ) line profiles during the present outburst in the HRS/SALT spectra (medium-resolution mode:  $R \sim 40000$ ) and two FEROS spectra taken during the 2005 outburst. The red dashed vertical lines mark the systemic velocity.

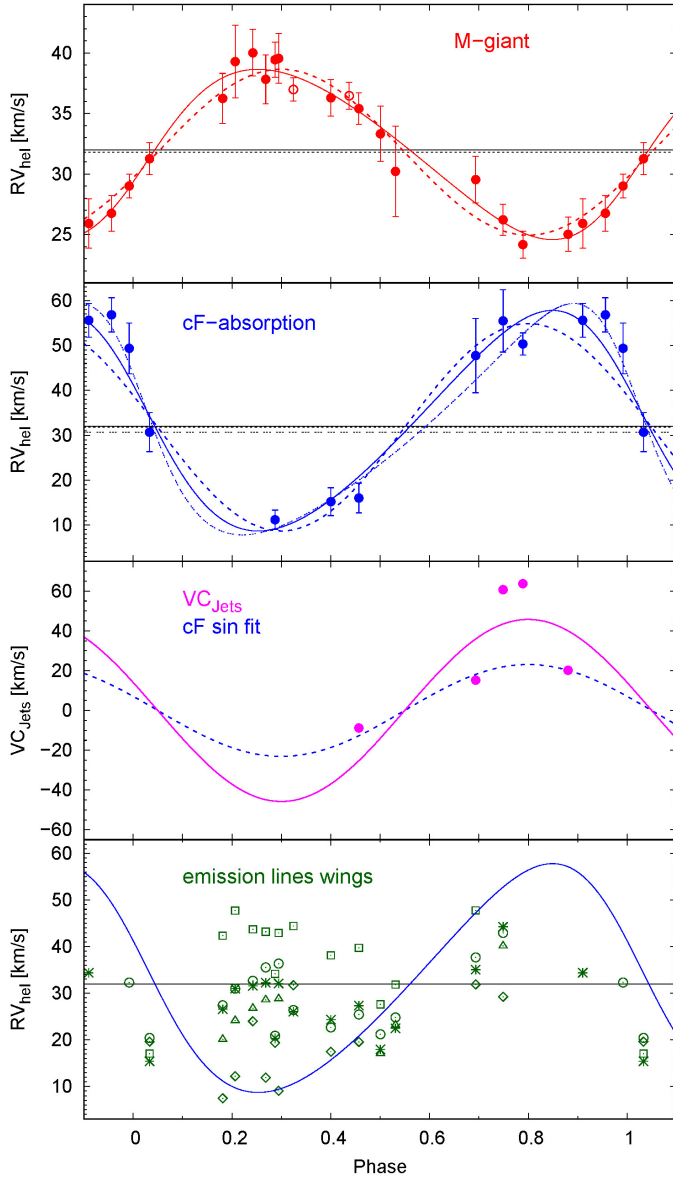


**Fig. A.5.** Radial velocity curves of the red giant (*top*) and hot (*middle*) components folded with period  $P_{\text{sp}} = 918^{\text{d}}$ . SALT/HRS and FEROS data are shown with filled and open circles, respectively. Solid lines show synthetic radial velocity curves for the case of the eccentric orbit and dashed lines in the case of a circular orbit. The horizontal lines represent the systemic velocities for the eccentric (solid) and circular (dashed) cases. The lower *middle* panel shows the jet centre velocity  $VC_{\text{J}}$ . The *bottom* panel presents the radial velocities of the emission line wings:  $\text{H}\alpha$  (circles),  $\text{H}\beta$  (diamonds),  $\text{He I } \lambda 5875.6 \text{ \AA}$  (asterisks),  $\text{He II } \lambda 5411.5 \text{ \AA}$  (triangles) and the mean value from  $\text{He I } \lambda 5875.6 \text{ \AA}$ , and  $\lambda 7065.2 \text{ \AA}$  lines (squares), respectively, compared to the radial velocity curve of the hot component (blue line). The method described by Shafter et al. (1983) and references therein were used to measure the velocities of emission lines wings.